EES Batteries

PAPER

View Article Online
View Journal | View Issue

Cite this: *EES Batteries*, 2025, **1**, 598

Quantifying silicon anode restructuring during calendar aging of lithium-ion batteries by plasma focused ion beam tomography and chemical mapping†

Joseph Quinn, *[a] Pavan Badami,[b] Qian Huang, [a] Chongmin Wang [c] and Daniel P. Abraham *[b]

To design high-performance lithium-ion batteries with Si anodes, it is critical to understand the underlying physical mechanisms that cause performance loss during aging. To quantify calendar aging losses, we conducted electrochemical tests on 3-electrode cells with a NMC811 cathode, a Si anode and a Li-metal reference electrode. As expected, these cells showed capacity decay and impedance rise over 8-months of testing. The impedance rise could be mainly attributed to the NMC811 cathode, except at low cell voltages wherein the Si anode is highly delithiated. Additional half-cell cycling tests with electrodes harvested from these aged cells revealed that a loss of lithium inventory (LLI) and a loss of active material (LAM) in the Si anode caused the loss in full-cell capacity. To elucidate loss mechanisms, we developed a technique that combined plasma focused ion beam (PFIB) tomography and energy dispersive X-ray spectroscopy (EDS)-based segmentation to visualize and quantify chemical and morphological properties of the electrode microstructure. These results revealed that aging led to increases in electrode thickness, electrode fragmentation, and quantity of solid electrolyte interphase (SEI). In addition, we used cryo-scanning transmission electron microscopy (STEM) imaging and electron energy loss spectroscopy (EELS) measurements to examine sub-nanometer changes in the Si particles on aging: the results showed increasing particle fragmentation and SEI formation on the newly created surfaces. This work provides a key insight into Si anode aging mechanisms through the development of a microstructure characterization technique that can resolve the various components within an electrode with the highest resolution to date.

Received 19th February 2025,
Accepted 17th April 2025

DOI: 10.1039/d5eb00036j

rsc.li/EESBatteries

Broader context

To develop high-energy battery materials, it is critical to understand the underlying mechanisms that cause systems to degrade over time. Performance losses caused by changes in the electrode microstructure are particularly significant since microstructures affect properties like conductivity and ion transport, which are critical to the basic function of the cell. In this work, we developed a characterization method to combine PFIB tomography and EDS mapping to investigate microstructural changes in electrodes before and after operation. Algorithms were developed to identify each component of the electrode within a sample volume to generate chemo-mechanical 3D reconstructions with the highest resolution to date. This technique was applied to study performance degradation in Si anodes whose use in lithium-ion batteries can improve capacity but lead to losses as the cells age over time. By quantifying microstructural properties of the silicon anodes before and after the aging process, we show the underlying mechanisms for degradation, which can be used to guide the design of systems with improved stability. This characterization technique provides key insights into the effect of the Si anode microstructure on performance and is widely applicable to alternative battery chemistries.

Introduction

To develop high-energy battery materials, it is critical to understand the underlying mechanisms that cause systems to degrade over time. Performance losses caused by changes in the electrode microstructure are particularly significant as these properties play an essential role in the basic function (such as ion transport and electronic conductivity) of battery systems. A wide variety of characterization techniques have

[a]*Energy and Environment Directorate, Pacific Northwest National Laboratory, Richland, WA 99354, USA. E-mail: joseph.quinn@pnnl.gov*
[b]*Chemical Sciences and Engineering Division, Argonne National Laboratory, Lemont, Illinois, 60439, USA. E-mail: abraham@anl.gov*
[c]*Environmental Molecular Sciences Laboratory, Pacific Northwest National Laboratory, Richland, Washington 99354, USA*

† Electronic supplementary information (ESI) available. See DOI: https://doi.org/10.1039/d5eb00036j

been applied to (1) quantify three-dimensional chemical and morphological properties of the electrode microstructure, (2) investigate how these properties change after operation, and (3) determine how microstructural properties ultimately affect system performance.[1,2] In battery electrodes some of the critical chemo-mechanical properties of the microstructure can only be observed at very high magnifications. One such example involves calendar aging of silicon nanoparticle-based anodes within lithium-ion batteries (LIBs). These anodes can store significant quantities of lithium but their performance degrades during calendar aging, which occurs when the cell ages in time (as opposed to cycling losses during the lithiation/delithiation processes).[3] While microstructural changes of calendar aged Si anodes likely have a critical impact on system performance, characterizing these effects is a significant challenge as critical properties, such as particle distribution and electrode porosity, require analysis at length scales below the maximum resolution of X-ray-based techniques such as micro or nano-computed tomography.[1]

Electron microscopy techniques can provide morphological information on electrode microstructures with sub-nanometer resolution.[1,4,5] One such technique is focused ion beam (FIB) or plasma focused ion beam (PFIB) tomography, which uses a scanning electron microscope (SEM) to image materials. However, the gray-scale image histograms obtained from these measurements can often be convoluted by the presence of multiple phases, material porosity, and beam-induced artifacts, making it difficult to resolve the relevant electrode components. Furthermore, these tomographs provide little information on material chemistry. By combining PFIB tomography with energy dispersive X-ray spectroscopy (EDS) mapping we can quantify the chemical and morphological properties of electrode materials.

In this work, we investigate the microstructural changes in Si anodes caused by calendar aging by developing a method to combine PFIB tomography and EDS mapping. Algorithms were developed to (1) align image stacks of multiple SEM images and EDS maps, (2) segment images to identify various electrode components within the sample volume to generate three-dimensional reconstructions of the microstructures, and (3) quantify properties of the electrode microstructure and correlate changes in these properties to losses in battery performance. In addition, we examined the morphological and chemical changes caused by calendar aging on single nanoparticles of Si using cryo-scanning transmission electron microscopy (Cryo-STEM) and electron energy loss spectroscopy (EELS). Our data reveal that capacity loss during calendar aging result from a combination of factors including loss of lithium inventory (LLI) caused by continuous solid electrolyte interphase (SEI) growth as well as loss of active material (LAM) caused by electrode swelling and a decrease in the connectivity of silicon particles. Mitigating these losses, through tailoring electrolyte chemistry and particle morphology, should increase the longevity of lithium-ion cells containing high-loading silicon anodes. The microstructure characterization technique developed in this work can be applied to a wide range of anode and cathode battery chemistries to investigate the effects of electrode microstructure on system performance.

Experimental

Materials and electrodes

The Si particles used to fabricate the cell anode were obtained from collaborators at the Oak Ridge National Laboratory (ORNL) and was produced as described in ref. 6 and 7. Briefly, powder produced by high-energy milling of Si boules was further milled with propylene carbonate (PC) that was intended to passivate the particle surfaces: the material was then dried at 250 °C to remove excess PC. The size of the milled Si particles was ~200 nm. The electrode, fabricated at Argonne's Cell Analysis Modeling and Prototyping (CAMP) facility, comprised a coating of this Si (80 wt%) along with C45 Timcal carbon additive (10 wt%) and polyimide P84 binder (10 wt%) cast onto a 10 μm thick Cu foil current collector: the laminates were heated for an hour at 350 °C in an Ar–gas environment to enable cross-linking of the P84 polymer.[8] After a light calendering, the electrode porosity was estimated as 57.2% and the areal capacity (1.0–0.01 V, C/25 rate) determined to be 2.3 mA h cm^{-2}. The cell cathode, also fabricated at CAMP, comprised a coating of commercial NMC811 ($LiNi_{0.8}Mn_{0.1}Co_{0.1}O_2$) powder (90 wt%), C45 carbon (5 wt%) and PVdF binder (5 wt%) on a 20 μm thick Al current collector. The electrode porosity was estimated as 34.5% and the areal capacity (2.5–4.3 V, C/25 rate) determined to be 3 mA h cm^{-2}. Before cell assembly, both electrodes (Si and NMC811) were dried at 110 °C for ~12 h in a vacuum oven to minimize their moisture contents.

Cell assembly and electrochemical testing

Our measurements were conducted using reference electrode cells assembled and tested in an Ar-atmosphere glovebox as described in ref. 9 and 10. Briefly, the cells contained NMC811 cathodes and Si anode discs (20.3 cm^{-2}) separated by two layers of Celgard 2320 separator discs (45.6 cm^{-2}). The electrolyte comprised 1.2 M $LiPF_6$ dissolved in 3 : 7 w/w solvent mixture of ethylene carbonate (EC) and ethyl methyl carbonate (EMC) and 3 wt% fluoroethylene carbonate (FEC) as the additive. The cells were flooded, with electrolyte content roughly 30 μL cm^{-2} of the electrode. The micro-reference electrode was created by *in situ* deposition of lithium from the NMC811 electrode onto a 1 mm exposed tip of a 25 μm dia. insulated Cu wire sandwiched between the separators.

All electrochemical cycling tests were performed at 30 °C using a MACCOR Series 4000 Test System. Prior to calendar aging, the cells were conditioned according to the protocol depicted in Fig. S1,† developed to ensure electrode wetting, prevent lithium-plating, and complete SEI formation on the Si anode. The calendar aging protocol depicted in Fig. S2† is based on the Open Circuit Voltage (OCV) – Reference Performance Test (RPT) developed for the United States Advanced Battery Consortium.[11] This protocol consists of 2

initial cycles at C/10 rate between a lower cutoff voltage (LCV) of 3.2 V and an upper cutoff voltage (UCV) of 4.2 V, OCV/RPT over a 30-day period which includes daily current pulses to measure impedance and a daily charge to restore cell voltage to its UCV, and a final cycle at C/10 rate. During the cycles, we instituted a LCV hold to minimize the effect of impedance during Si delithiation (cell discharge). The protocol was repeated multiple times to examine cell performance degradation over several months. In addition, before and after calendar aging, we included a modified version of the hybrid pulse power characterization (HPPC) test; this test contains charge and discharge current pulses and is used to measure impedance changes during cell aging.[12] Note that the C-rates listed in this manuscript are based on the initial C/1 capacity of cells cycled in the 3.2–4.2 V range; these rates are not revised to account for cell capacity loss during cycling. Also, the *initial* negative-to-positive electrode capacity (N/P) ratio in the cycling window was 1.3; the manner by which we determined the N/P ratio is described elsewhere.[13] Accounting for all measurements, the cells examined this study were tested over a ~8-month period: during this time they experienced ~210 days of OCV after full charge and ~32 full charge/discharge cycles.

After completion of aging tests, the cells were disassembled in an Ar-atmosphere glove box and electrodes harvested for electrochemical and electron microscopy studies. For electrochemical characterization, harvested electrodes were assembled into half cells with a Li metal counter electrode, fresh electrolyte, and fresh separator. The Si electrode half cells were cycled between 0.05–1.0 V, and the NMC811 half cells between 2.5–4.3 V, to determine electrode capacity loss that resulted from full cell aging.

SEM/PFIB microstructure data acquisition

The Si anode samples were prepared for PFIB tomography in an Ar-atmosphere glove box. To avoid air-exposure sections of the sample were mounted on an SEM stub and transferred to the PFIB/SEM load lock using a Thermo QuickLoader. The PFIB used an inductively coupled Xe^+ plasma source. To prepare samples for tomography a ~3–5 μm Pt layer was deposited on the surface of the characterized volume: the sample was then milled with the PFIB to expose the electrode cross-section. The three-dimensional data acquisition process was performed with Thermo AutoSlice and View software and consisted of alternating steps of SEM/EDS imaging and PFIB slicing. For cycled electrodes, the SEM imaging was performed at 2 kV and 0.1 nA, while EDS mapping was performed at 5 kV and 3.2 nA. The pristine electrode was characterized with a single beam setting of 5 kV and 13 nA. The PFIB milling was performed using a beam current of 15 nA with a 200 nm step size. The data acquisition process resulted in multiple image stacks where each slice is represented by two sets of SEM images (one for each beam setting) and six EDS maps for the elements Si, O, F, Cu, C, and Pt.

Image processing to generate 3D reconstructions

The raw image stacks need to undergo alignment and segmentation to create 3D reconstructions of the sample volume. The alignment was executed to (1) prevent the electrode cross-sections from shifting in every frame and (2) align each slice's multiple sets of SEM images and EDS maps. The low-kV SEM image stack was used to perform frame-by-frame alignment of the electrode cross section. To make an initial alignment, a feature on the electrode cross section was selected with a point and click method for each image. The alignments were then fine-tuned using image registration algorithms from MATLAB's Image Processing Toolbox. In this step automated alignments were performed on a selected area of electrode cross section (usually at the Cu–Si interface). To align the high-kV SEM images to the (frame-by-frame aligned) low-kV SEM image stack, a similar two-step alignment process performed using a point and click feature alignment followed by fine-tuning using an automated image registration algorithm. In this process, every image transformation that was implemented on the high-kV SEM images was saved and applied to each EDS map of every slice. To generate 3D reconstructions from the aligned SEM images and EDS maps, a segmentation process was developed to identify the phases present at every voxel throughout the 3D volume. In this sample set the relevant phases are the Si particles, SEI/binder components (C/O/F), pore space, and the copper current collector. The Si, SEI/binder, and Cu phases were identified by comparing the strength of the EDS signal at every voxel and were assigned based on the highest number of counts. Pore space was quantified using two different methods. Small pores were identified with gray thresholding from the low-kV SEM images, where void space is identified as the darkest areas of the image. It is more difficult to perform gray thresholding in FIB tomography for large void spaces because the back of a large pore can have the same brightness value as the rest of the electrode cross-section; this would artificially reduce pore space in the reconstructed 3D volume. However, due to the sample geometry, SEM beam, and EDS detector, these large pores have a very low total EDS counts due to signal shadowing. By quantifying the local EDS counts and comparing them to the highest counts at the cross-sectional surface, large pores were identified by establishing an "EDS signal threshold". This new method to identify large pore spaces addresses a known weakness in FIB tomography analyses.

3D volume property quantification

After segmentation the phases were quantified at every voxel throughout the reconstruction. This quantification allows us to investigate how key properties of the microstructure, including Si surface area, electrode thickness, and SEI growth, change during calendar aging. MATBOX[14] was used to perform the quantification analysis and the MATLAB Image Processing Toolbox was used for 3D volume visualization.

Cryo-STEM and EELS analysis

To investigate changes to Si particles at the sub-Angstrom scale, scanning transmission electron microscopy (STEM) was performed on a 300 kV monochromated FEI Titan TEM with a probe aberration corrector. Electron energy loss spectroscopy

(EELS) was performed on a Gatan Image Filter (GIF)-Quantum spectrometer with an energy resolution of ~1 eV, a dispersion of 0.05 eV per ch and a pixel width of ~2–3 nm. The dwell time was 10 ms for the cycled samples and 50 ms for the pristine electrode. The EELS analysis was performed with a power law background model, the Li K-edge was analyzed with a Hartree-Slater cross-section model, the Si-$L_{2,3}$-edge was analyzed with Si and SiO_2 standards as the cross-sectional model. All spectrums were corrected for plural scattering. EDS elemental mapping was performed with an Oxford Instruments AZTEC X-Max detector.

Results

Electrochemical testing

Representative voltage *vs.* capacity profiles as a function of time from the electrochemical tests are shown in Fig. 1a–c. The plots before calendar aging (solid lines), show that the cell voltage hysteresis (Fig. 1a) arises from the Si anode (Fig. 1c): minimal hysteresis is seen in the NMC811 profile (Fig. 1b). Observe that when the cell is cycled between 3.2–4.2 V, the NMC811 potential varies between 3.72–4.25 V while the Si electrode potential varies between 0.52–0.05 V.

Cell capacity decreases during calendar aging: the values changed from 1.8 to 1.26 mA h cm^{-2}, a decrease of 0.54 mA h cm^{-2} after 8-months of testing. Observe that the electrode cycling windows are very different after aging, even though the cell voltage limits are the same (see dashed lines in Fig. 1a–c). That is, even though the cell cycling window remains between 3.2–4.2 V, the NMC811 potential varies between 3.84–4.34 V while the Si electrode potential varies between 0.64–0.14 V. The upper and lower cycling potential of the NMC811 electrode (Fig. 1b) increases by 0.09 V and 0.12 V, respectively, indicating increasing oxide delithiation with aging: as oxide degradation increases with increasing delithiation, cycling at increasingly higher potentials is detrimental to electrode performance. The cycling potentials of the Si anode also increase; it is evident from Fig. 1c that the electrode is lithiated to a smaller extent but delithiated to a larger extent. In principle, the smaller lithiation would reduce the extent of Si swelling[15] and electrolyte reduction, while the larger delithiation would increase the likelihood of SEI dissolution reactions.

Cell impedance (Fig. 1d) also rises during aging: the magnitude of this increase varies depending on the voltage at which the current pulse is applied. At higher voltages (3.6–4.1 V), the increase is about 27 Ω cm^2 (64%) and arises from the NMC 811 electrode (Fig. 1e). At lower voltages (<3.5 V), the sharp impedance rise of the aged cell can be attributed to delithiation of the Si electrode (Fig. 1f). At these cell voltages, the Si electrode potential is >0.45 V *vs.* Li/Li^+ (Fig. 1c) and the active particles are being transformed from Li_xSi to Si. The rise in electrode impedance can be attributed to the increasing number of Si particles, which have both lower electronic and ionic conductivity.[15]

To identify sources of cell performance loss we disassembled the aged cells and reassembled the "harvested" electrodes in cells with Li–metal (see Experimental): representative data from these cells are shown here. The capacity of an aged NMC811 electrode is very similar to that of an as-prepared electrode (see Fig. S3†), indicating that cathode degradation is not a major contributor to cell capacity fade. In contrast, a harvested Si electrode (Fig. 2a) has ~0.3 mA h cm^{-2} lower capacity than its as-prepared counterpart, indicating a loss of active material in the aged electrode.[16] In addition, the $Li_{15}Si_4$ peaks[17] that are prominent in the as-prepared electrode are absent in the aged electrode (Fig. 2b). These electrode performance differences could result from a variety of causes, including Si particle morphology changes, electrode restructuring, and increased SEI formation during aging; these causes are explored with the PFIB tomography, EDS mapping, cryo-STEM and EELS studies described below.

PFIB/EDS electron microscopy characterization

As described above in the Experimental section a method was developed to combine PFIB tomography with EDS mapping to generate chemo-mechanical 3D reconstructions of the electrode microstructures. In brief, PFIB/SEM was used to take cross-sectional images at numerous slices through a 3D volume of the samples. Each slice was characterized with two sets of SEM images (Fig. 3a and b) and a set of EDS maps for Si, O, C, F, Pt, and Cu (Fig. 3c–h). All images were aligned frame-by-frame (Fig. 3i), followed by a segmentation process to determine identity of phases (Si, SEI/binder, Cu, pore space) at every voxel within the 3D reconstruction (Fig. 3j).

The segmented images enable the 3D visualization of individual phases within the microstructure for electrodes at various stages of calendar aging. Fig. 4 shows 3D reconstructions for pristine electrodes, electrodes after conditioning cycles, and electrodes after 8-months of aging. For each sample in Fig. 4, reconstructions were made to highlight the overall electrode morphology, as well as each individual electrode component including the Si particles, SEI/Binder, pore/void space, and the Cu current collector. For the electrodes after conditioning and aging cycles, increased voids are observed near the Cu current collector interface (Fig. 4i and n): these voids are not observed in the pristine electrode cross-section (Fig. 4d). This voids could be the consequence of high stresses developed at the coating/Cu interface because of electrode volume changes during the Si lithiation/delithiation;[18] these stresses weaken adhesion at this interface and in some cases can also rip apart the Cu foil (for example, see Fig. 4j).

By analyzing the phases individually, the data in Fig. 4 can be used to quantify properties of the microstructure that are critical to cell performance. The effects of calendar life on the electrode microstructure can be determined by comparing the quantified properties before and after the aging process. MATBOX, an open-source microstructure analysis tool, was used for the quantification calculations. There were several properties that showed significant changes after aging including: electrode thickness, SEI growth, silicon connectivity, and silicon surface area.

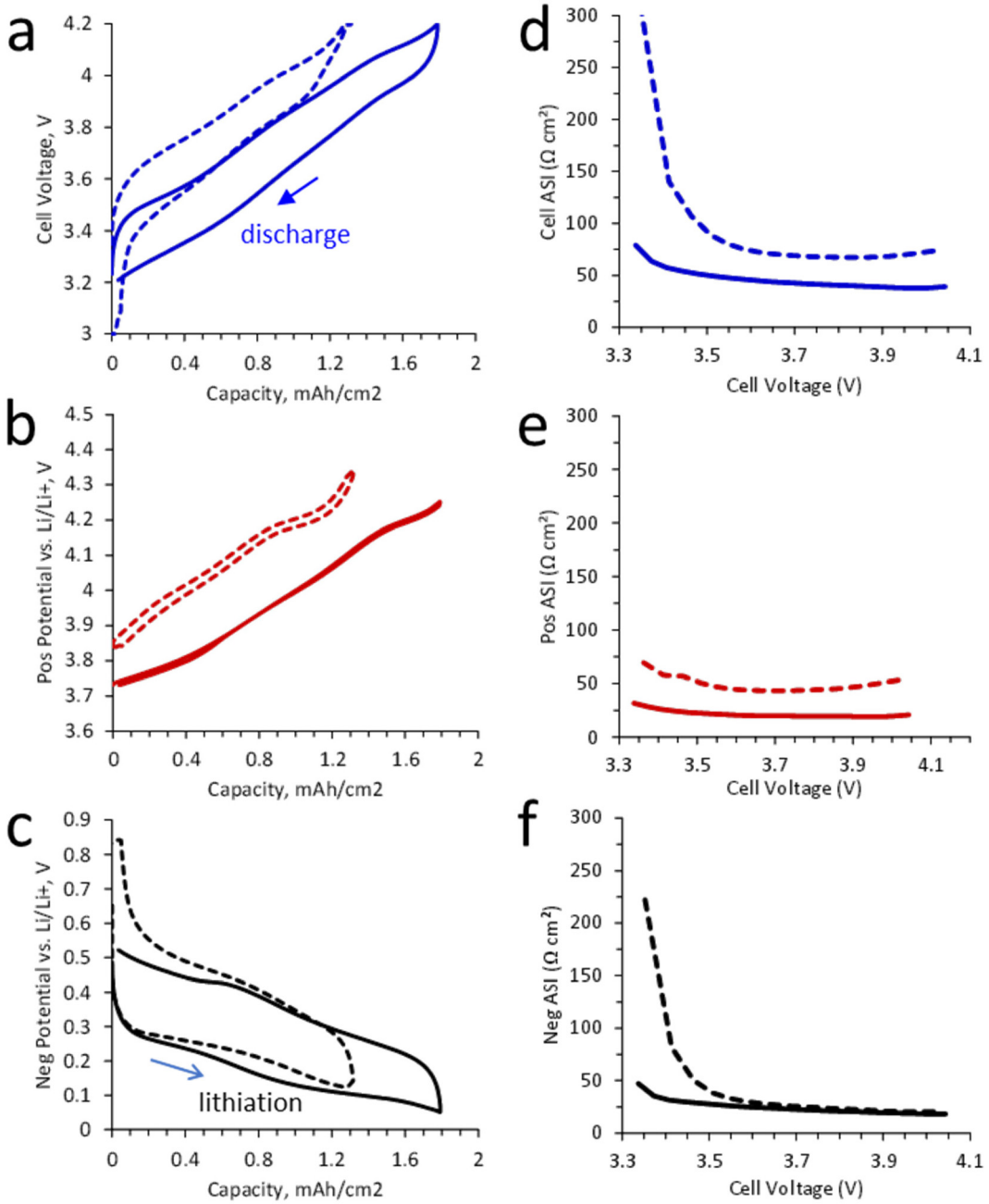

Fig. 1 Voltage profiles and impedance Plots from the 3-electrode cells. (a) Voltage profiles from a NMC811/Si cell before (solid lines) and after (dashed lines) 8-months of testing. Corresponding profiles of the NMC811 and Si electrodes are in (b) and (c) respectively. (d–f) show Area Specific Impedance (ASI) *vs.* cell voltage plots for the cell, NMC811, and Si electrode, respectively before (solid lines) and after (dashed lines) calendar aging; the measurements were conducted at 30 °C using 3 C, 10 s pulses.

Fig. 4a, f, and k show that there is an increase in electrode thickness after the conditioning cycles and after calendar aging. The thicknesses of the various electrodes were ~19 μm for the pristine state, ~25 μm after conditioning cycles, and ~34 μm after calendar aging. The segmented 3D reconstructions shown in Fig. 4c, h, and m show that the increase in electrode thickness is due to a large increase in the volume of the SEI/Binder components. The volume of the SEI/binder components per unit area (Fig. 5b), is initially very low for the pristine electrode (which only has binder) and increases after conditioning cycles and after calendar aging. As the binder content is unchanged, the data indicate that the thickness increase is caused by continued deposition of electrolyte reduction products (SEI formation) in the electrode pores. Such deposition is to be expected as the SEI formed during silicon expansion sloughs off the particles during delithiation and accumulates in the electrode pores.

Connectivity is a property that has previously been used in microstructure analysis as a measure of the particle

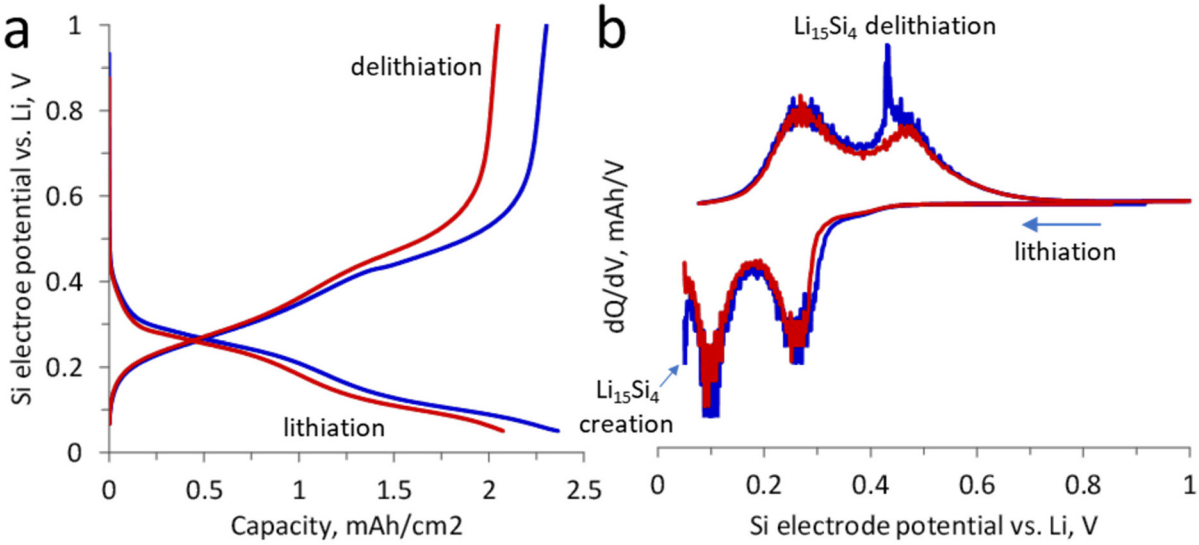

Fig. 2 Data from pristine and harvested Si electrodes. (a) Potential profiles of an as-prepared Si electrode (blue) and an electrode harvested from a cell after 8-months of aging (red), cycled in cells with a Li-metal counter electrode. (b) Differential capacity *vs.* Si electrode potential plots derived from the data in (a).

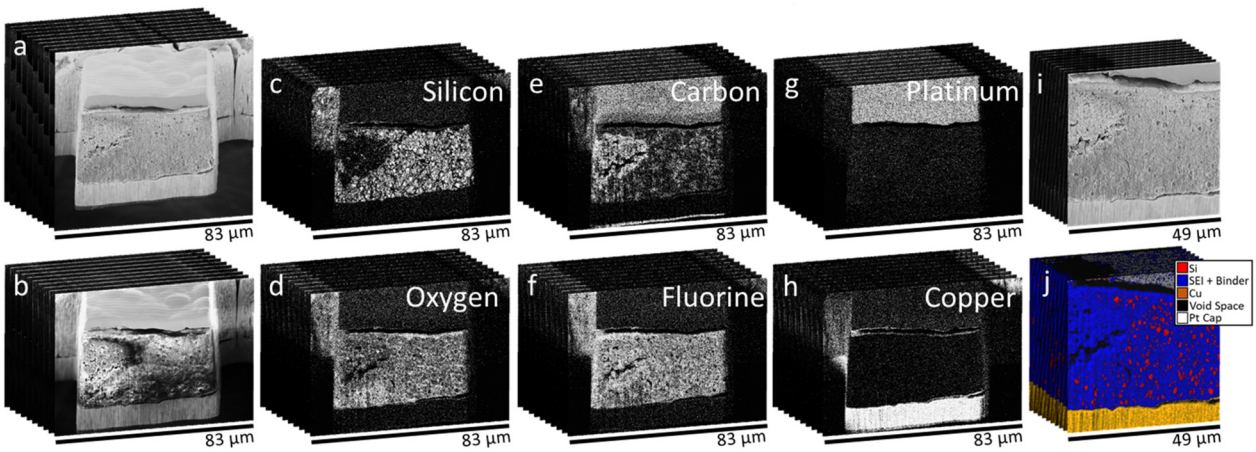

Fig. 3 Alignment and segmentation process to create 3D reconstructions from PFIB tomography with EDS elemental map integration (limited slices shown). (a) SEM image stack with low-kV beam settings for morphological analysis. Each image represents a slice from the 3D sample volume. (b) SEM image stack with high-kV beam settings used for elemental mapping. (c–h) Stacks of EDS elemental maps for Si, O, C, F, Pt, and Cu. (i) Low-kV SEM image stack with frame-by-frame cross-sectional alignment. (j) Stack of segmented images that identify various electrode components including Si nanoparticles, SEI/Binder, Cu current collector, pore space, and the Pt cap.

distribution.[14,19] Multiple voxels of the same phase that share face-to-face contact are grouped into "clusters". The isotropic definition of connectivity measures the percentage of separated clusters (physically separated from other clusters) in comparison to the percentage of large/edge clusters. In other words, a high percentage of physically separated clusters can quantify the amount of Si fragmentation in the calendar aged anode. MATBOX was used to quantify Si connectivity for each of the Si anode samples. Fig. 6a–c depict 3D reconstructions of the various electrodes showing only the silicon particles, where each color represents a separate connected particle cluster. Thus, the abundance of distinct colors in the calendar aged electrode (Fig. 6c) means that there are numerous physically separate Si clusters. It is evident that fragmentation of the electrode increases during aging. The amount of fully separate clusters (not large or edge clusters) is quantified in Fig. 5c: note there is a ~7× increase in separate clusters between the conditioned and the calendar aged electrode.

Particle surface area is a key property of the electrode microstructure since high surface area can lead to increased direct Si-electrolyte contact leading to increased SEI formation. Fig. 5d shows that there is a large increase in surface area after the conditioning cycles and another increase after calendar

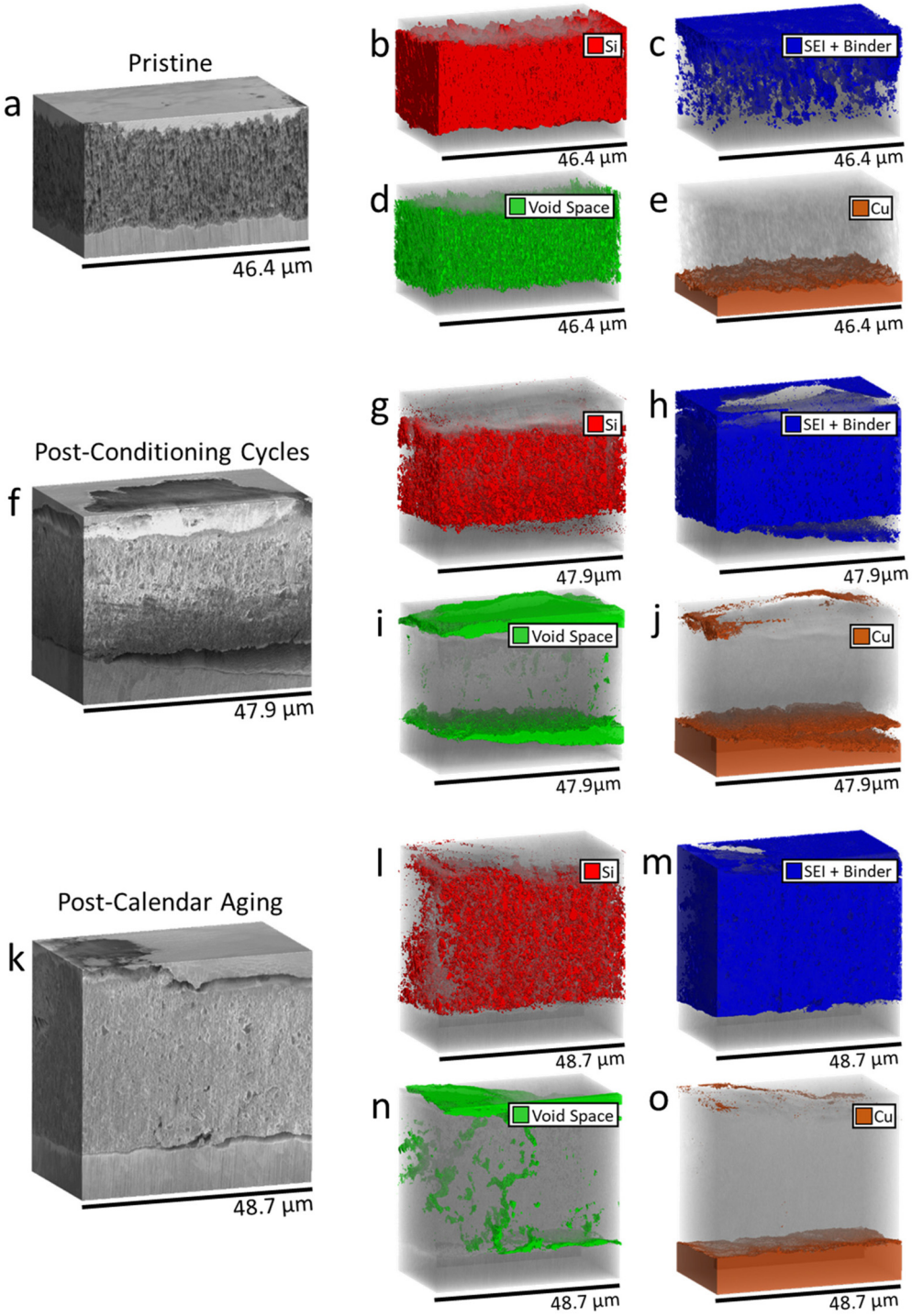

Fig. 4 3D reconstructions of the silicon anodes at the various stages of aging. Data for the pristine electrode (a–e), electrode after conditioning cycles (f–j), and electrode after calendar aging (k–o). (a), (f), and (k) depict the overall morphology using the low-kV SEM image data. All other reconstructions analyze the individual electrode components within the 3D volume including the Si particles (b, g and l), the SEI/Binder (c, h and m), void space (d, i and n), and the Cu current collector (e, j and o). The apparent Cu intensity in the Pt layer of (j and o) is an artifact of the mapping procedure.

aging. The increase in surface area is due to the Si–Li bond breaking/reformation that occurs during the silicon lithiation/delithiation cycles. The consequence of the surface area increase is shown in Fig. 4c, h, m and 5b, wherein the aged electrodes show an increase in thickness due to the deposition of electrolyte reduction products. These SEI products form between the Si clusters and can cause both electronic and ionic isolation of previously-active particles.

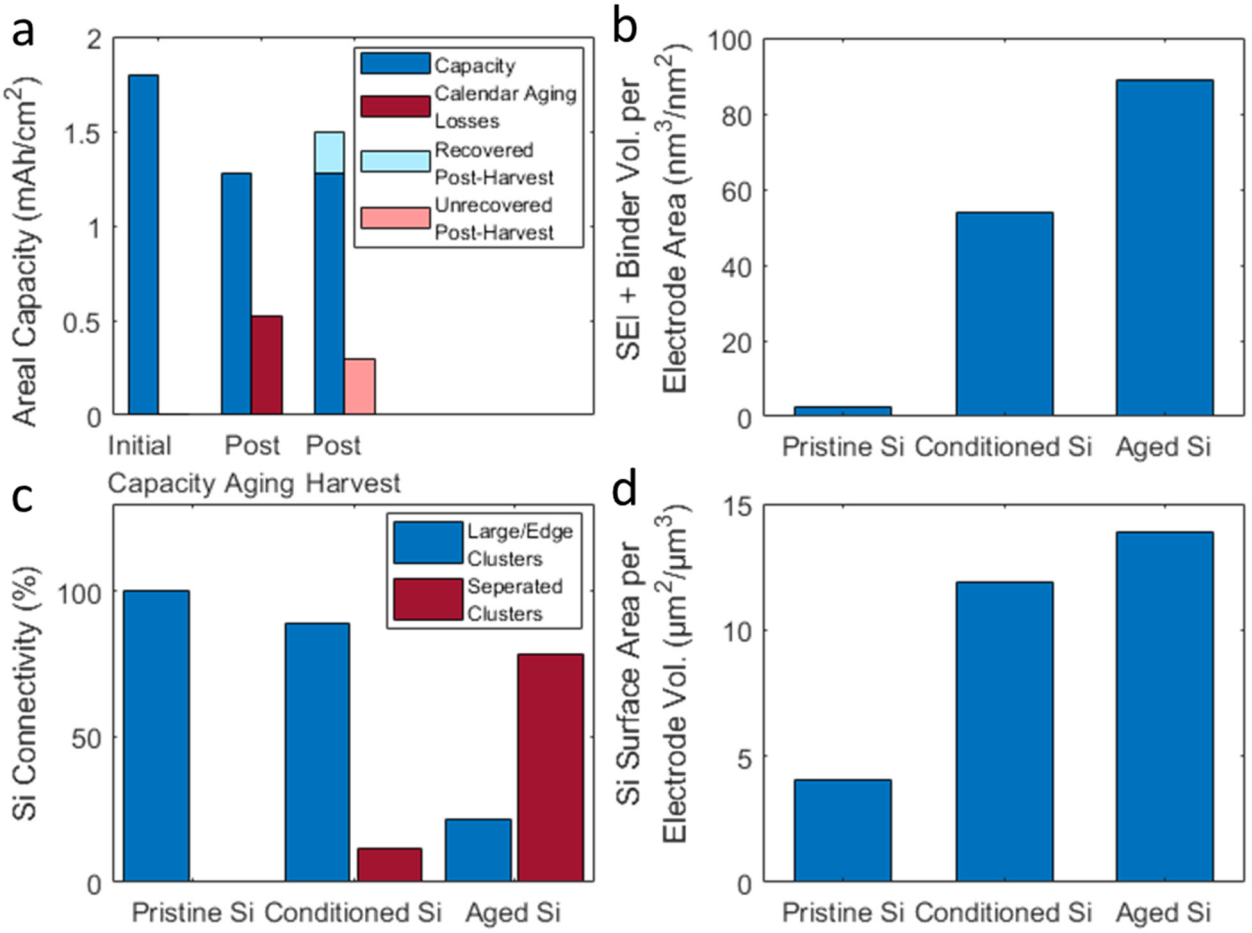

Fig. 5 Quantification of electrochemical and microstructural properties for the electrodes in various stages of the calendar aging process. (a) Shows areal capacity of electrodes after the initial conditioning cycles, after calendar aging, and after the lithium inventory was replenished in harvested electrodes. (b–d) Property quantification for the 3D reconstructions at various stages of the calendar aging. These properties include (b) SEI + Binder volume (normalized by area), (c) Si particle connectivity, and (d) Si particle surface area.

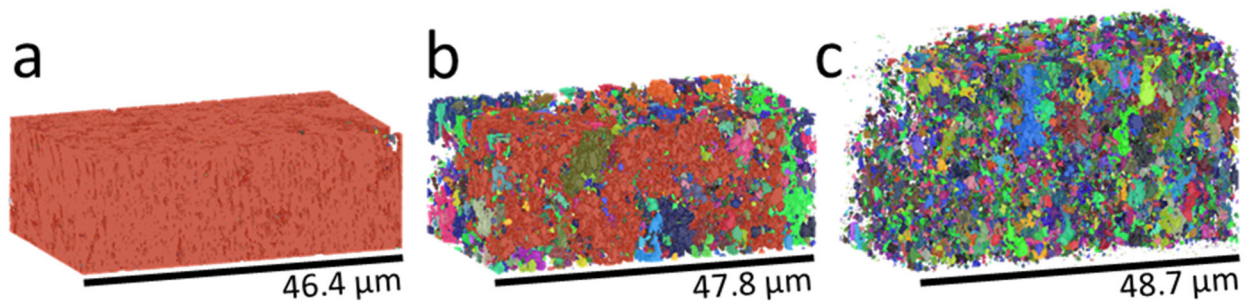

Fig. 6 3D reconstructions depicting Si particle connectivity at the various stages of aging. Each reconstruction shows silicon nanoparticles for the (a) pristine electrode, (b) electrode after conditioning cycles, and (c) electrode after calendar aging. Each color in (a–c) represents a separate connected cluster, *i.e.*, the more colors, the more separated the Si clusters.

Cryo-STEM/EELS for single particle-scale Si/SEI characterization

Cryo-STEM and EELS were used to investigate nanoscale changes caused by calendar aging at a single particle level. STEM imaging was used to observe morphological changes, while EDS and EELS were used to investigate the spatial distribution of the elements and chemical composition. Annular dark field (ADF) images on representative Si particles in the pristine state, after conditioning, and after 8-months of calen-

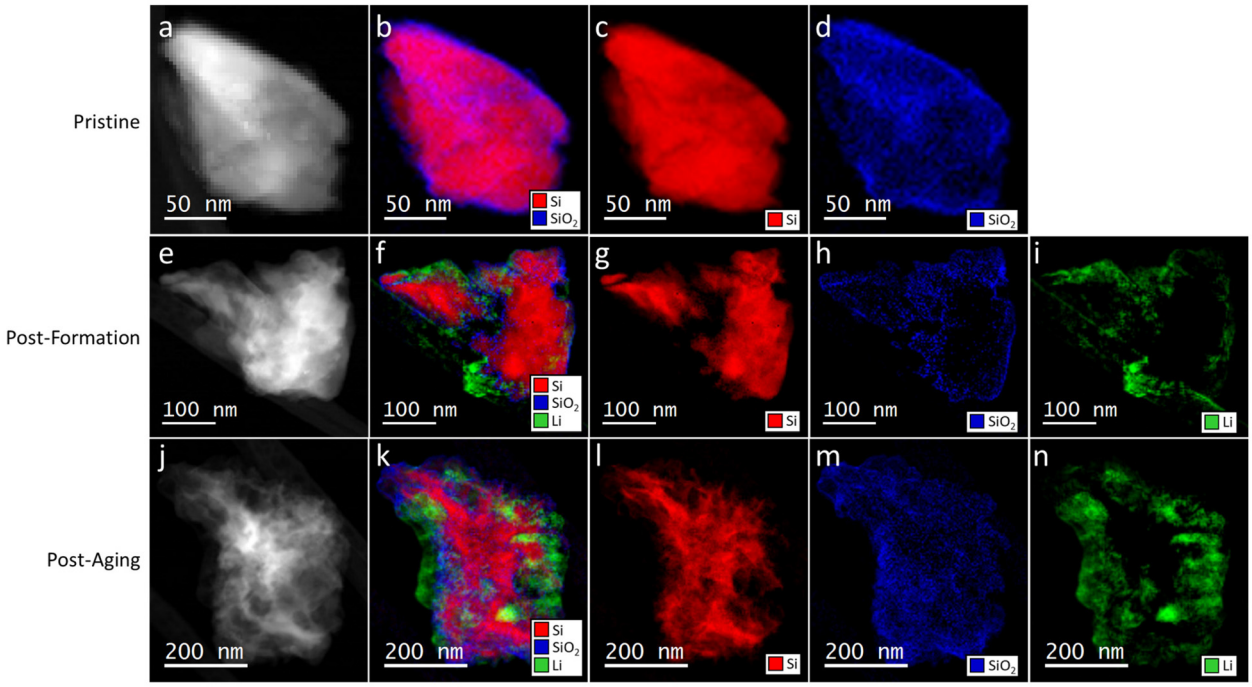

Fig. 7 ADF and Cryo-EELS maps of Si nanoparticles at the various stages of calendar aging. (a) ADF and (b–d) EELS maps of a silicon particle from a pristine electrode. (e) ADF and (f–i) EELS maps of a Si particle from an electrode after conditioning cycles. (j) ADF and (k–n) EELS maps for a Si particle after calendar aging.

dar aging are shown in Fig. 7a, e and j respectively. The images show that the Si particles transform from a rock-like structure to a cotton candy-like structure on aging. This transformation occurs because of the formation and breaking of Li_xSi bonds and results in the increased surface observed in Fig. 5d. Corresponding EELS maps showing the distribution of Si, SiO_2, and Li are in Fig. 7b–d, f–i and k–n. The Si and SiO_2 maps are consistent with increasing fragmentation of the particles. The Li maps are from SEI species, which could include LiF, Li_2O, Li_xSiO_y, Li_xPO_y, Li alkyl carbonates, on and within the particles.[20,21] Additional STEM images and EDS maps of Si nanoparticles from the various electrodes are provided in Fig. S4–S6.† In addition to Si and O, the maps show the presence of Li, C, F and P, which are all components of the electrolyte and expected in the SEI. These maps show that the SEI elements are present throughout the cycled/aged samples. Particle amorphization and accumulation of intra-particle SEI would change the stress dynamics of particles, which likely prevents formation of the $Li_{15}Si_4$ phase in aged electrodes (Fig. 2b).

Discussion

To improve longevity of LIB cells it is critical to understand the underlying physicochemical mechanisms that lead to performance loss during aging. An important question regarding the aging mechanism is whether cell capacity loss caused by a loss in lithium inventory (LLI) or a loss in active material (LAM). LLI-type losses occur when lithium is consumed during operation until there is an insufficient quantity to maintain capacity. LAM losses occurs when the active material itself can no longer participate in lithiation/delithiation reactions as it did initially. Multiple physical mechanisms can lead to LAM-type losses including particle degradation leading to electronic or ionic isolation and particle dissolution leading to less active material available to hold charge.

In this work, we designed an electrochemical test protocol (Fig. S2†) to determine the effect of calendar aging on LIB cells with NMC811 cathodes and Si anodes. The protocol caused cell capacity to decrease from ~1.8 to ~1.26 mA cm^{-2}, a loss of 0.54 mA cm^{-2} (Fig. 5a). To deconvolute the contributions of LLI and LAM to capacity loss we harvested Si anodes from disassembled cells and cycled them in new cells with a lithium metal counter electrode. These data indicated that LAM and LLI losses in the aged Si electrode were ~0.3 mA h cm^{-2} and ~0.24 mA h cm^{-2}, respectively.

To determine reasons for these LAM and LLI losses we compared PFIB tomography and analytical electron microscopy results from Si anode samples in the pristine state, after conditioning cycles, and after calendar aging. Microstructural properties were calculated from the 3D reconstructions (Fig. 5) described above. The LLI and LAM-type losses after aging can be directly attributed to nanoscale changes in the Si particles and microscale changes in the electrodes.

The large increase in electrode thickness can be attributed to deposition of electrolyte reduction products that increase the volume per area of the SEI. As electrolyte reduction

involves the trapping of Li^+ ions within inorganic (LiF and Li_2O) and organic (Li alkyl carbonates) components,[22,23] continued SEI formation directly leads to LLI through the irreversible generation of un-cyclable lithium species. This SEI growth is proportional to the increased exposed area of surface nanoparticles, which occurs even in the absence of cycling and explains the capacity loss during calendar-aging. Continuous SEI deposition at the Si anode could be minimized by altering cell voltage limits, which can affect the identity and rate of the deposited species[24,25] and can decrease electrode volume changes. SEI deposition can also be reduced by using electrolyte compositions that are less prone to reduction, and by limiting electrolyte solvent transport to the reducing surface sites through appropriate particle coatings.

Si connectivity, a metric for LAM-type losses, is quantified in Fig. 5c and visually depicted in Fig. 6. The results show a significant loss in Si connectivity both after the conditioning cycles and after calendar- aging. The fragmented Si clusters observed in Fig. 6 are apparently a consequence of electrode volume changes that occur during the electrode cycling: this fragmentation is accentuated by SEI deposited in the electrode pores. Portions of the electrode can be isolated and unable to participate in electrochemical reactions because of physical disconnection from the electron conduction network that could occur during the changes in electrode volume. In addition, chemical disconnection can result from the presence of an insulating SEI that hinders electron and/or Li^+ ion transport to the clusters. Disconnection can also result from silicon particle degradation at the sub-nanometer scale (Fig. 7). The continued configurational changes within particles that result from the creation and breaking of Li–Si bonds continually fragment the particles, increasing intra-particle porosity and creating a fluffy morphology (Fig. 7j). Electrolyte reactions with the newly created surfaces can both deplete Li-inventory through SEI formation and deplete solvent/salt constituents of the electrolyte,[26] which in the long-term can cause "rollover failure" of the cells.[27] The results suggest that capacity losses can be mitigated by designing systems that reduce Si particle isolation during calendar aging. This could be achieved by improving the design of electrode architecture to accommodate electrode volume expansions as exemplified in ref. 28 and 29 and to constrain Si particle fragmentation.

Conclusions

A technique combining PFIB tomography and EDS-based segmentation was developed to quantify chemical and morphological changes in Si anodes from calendar-aged lithium-ion cells. Results from the electrochemical behavior of the cell indicated that the cell capacity loss during aging was caused by a combination of LLI and LAM-type losses in the Si anodes. Microstructural data obtained on sample cross-sections showed a significant increase in thickness on aging, resulting from accumulation of SEI in the electrode pores. The LLI-type losses can be attributed to this SEI buildup, which results from electrolyte reduction reactions that trap (previously mobile) Li^+ ions. 3D reconstructions of the microstructure revealed fragmentation of the anodes and a consequential decline in Si particle connectivity, accentuated by the increase in SEI between particle clusters. This decrease in particle connectivity, along with the enhanced intra-particle Si fragmentation and SEI growth revealed by STEM/EELS studies, can cause the observed LAM-type losses. Our results highlight the need for improved electrolyte formulations that can minimize SEI growth reactions, different Si particle designs to confine its volume expansion, and alternative electrode designs and cycling protocols that would curtail expansion/contraction and mitigate fragmentation. The characterization methods described in this study provide mechanistic insights into the effects of the electrode microstructure on cell performance and are applicable to batteries containing various anode and cathode materials.

Data availability

The data supporting this article have been included in the main text or in ESI.† The analysis software MATBOX used for microstructure property quantification is publicly available at: **https://www.nrel.gov/transportation/matbox.html**.

Conflicts of interest

There are no conflicts of interest to declare.

Acknowledgements

This research was supported by the U.S. Department of Energy's Vehicle Technologies Office (VTO) under the Silicon Consortium Project, directed by Brian Cunningham and managed by Anthony Burrell. The electron microscopy work was carried out by using microscopes that are funded in part by a grant from the Washington State Department of Commerce's Clean Energy Fund. Part of the work was conducted at the William R. Wiley Environmental Molecular Sciences Laboratory (EMSL), a national scientific user facility sponsored by DOE's Office of Biological and Environmental Research and located at Pacific Northwest National Laboratory (PNNL). PNNL is operated by Battelle for the U.S. Department of Energy under Contract DE-AC05-76RL01830. The electrodes used in this article are from Argonne's Cell Analysis, Modeling and Prototyping (CAMP) Facility, which is fully supported by the VTO. Argonne National Laboratory, a U.S. Department of Energy Office of Science Laboratory, is operated by UChicago Argonne, LLC under Contract No. DE-AC02-06CH11357. The U. S. Government retains for itself, and others acting on its behalf, a paid-up nonexclusive, irrevocable worldwide license in said article to reproduce, prepare derivative works, distribute copies to the public, and perform publicly and display publicly, by or on behalf of the Government.

References

1 T. L. Burnett, R. Kelley, B. Winiarski, L. Contreras, M. Daly, A. Gholinia, M. G. Burke and P. J. Withers, *Ultramicroscopy*, 2016, **161**, 119–129.
2 R. F. Ziesche, T. M. M. Heenan, P. Kumari, J. Williams, W. Li, M. E. Curd, T. L. Burnett, I. Robinson, D. J. L. Brett, M. J. Ehrhardt, P. D. Quinn, L. B. Mehdi, P. J. Withers, M. M. Britton, N. D. Browning and P. R. Shearing, *Adv. Energy Mater.*, 2023, **13**, 2300103.
3 J. D. McBrayer, M.-T. F. Rodrigues, M. C. Schulze, D. P. Abraham, C. A. Apblett, I. Bloom, G. M. Carroll, A. M. Colclasure, C. Fang, K. L. Harrison, G. Liu, S. D. Minteer, N. R. Neale, G. M. Veith, C. S. Johnson, J. T. Vaughey, A. K. Burrell and B. Cunningham, *Nat. Energy*, 2021, **6**, 866–872.
4 C. Zhu, S. Chen, K. Li, Z.-W. Yin, Y. Xiao, H. Lin, F. Pan and L. Yang, *Sci. Bull.*, 2023, **68**, 408–416.
5 M. Zhang, M. Chouchane, S. A. Shojaee, B. Winiarski, Z. Liu, L. Li, R. Pelapur, A. Shodiev, W. Yao, J.-M. Doux, S. Wang, Y. Li, C. Liu, H. Lemmens, A. A. Franco and Y. S. Meng, *Joule*, 2023, **7**, 201–220.
6 J. Cai, X. Zhou, T. Li, H. T. Nguyen, G. M. Veith, Y. Qin, W. Lu, S. E. Trask, M.-T. F. Rodrigues, Y. Liu, W. Xu, M. C. Schulze, A. K. Burrell and Z. Chen, *ACS Appl. Mater. Interfaces*, 2023, **15**, 48085–48095.
7 K. G. Araño, B. L. Armstrong, E. Boeding, G. Yang, H. M. I. Meyer, E. Wang, R. Korkosz, K. L. Browning, T. Malkowski, B. Key and G. M. Veith, *ACS Appl. Mater. Interfaces*, 2023, **15**, 10554–10569.
8 J. Choi, K. Kim, J. Jeong, K. Y. Cho, M.-H. Ryou and Y. M. Lee, *ACS Appl. Mater. Interfaces*, 2015, **7**, 14851–14858.
9 A. Verma, M. C. Schulze, A. Colclasure, M.-T. F. Rodrigues, S. E. Trask, K. Pupek, C. S. Johnson and D. P. Abraham, *J. Electrochem. Soc.*, 2023, **170**, 070516.
10 M. Luo, M.-T. F. Rodrigues, L. L. Shaw and D. P. Abraham, *ACS Appl. Energy Mater.*, 2022, **5**, 5513–5518.
11 J. P. Christophersen, *Battery Test Manual For Electric Vehicles, Revision 3*, Idaho National Lab. (INL), Idaho Falls, ID (United States), 2015.
12 D. P. Abraham, D. W. Dees, J. Christophersen, C. Ho and A. N. Jansen, *Int. J. Energy Res.*, 2010, **34**, 190–203.
13 M.-T. F. Rodrigues, A. Y. R. Prado, S. E. Trask, S. Ahmed, A. N. Jansen and D. P. Abraham, *J. Power Sources*, 2020, **477**, 229029.
14 F. L. E. Usseglio-Viretta, P. Patel, E. Bernhardt, A. Mistry, P. P. Mukherjee, J. Allen, S. J. Cooper, J. Laurencin and K. Smith, *SoftwareX*, 2022, **17**, 100915.
15 A. Y. R. Prado, M.-T. F. Rodrigues, S. E. Trask, L. Shaw and D. P. Abraham, *J. Electrochem. Soc.*, 2020, **167**, 160551.
16 E. Wang, M.-T. F. Rodrigues, S. Park, F. Dogan and B. Key, *J. Power Sources*, 2024, **604**, 234477.
17 D. S. M. Iaboni and M. N. Obrovac, *J. Electrochem. Soc.*, 2015, **163**, A255.
18 M.-T. F. Rodrigues, S. Rajendran, S. E. Trask, A. R. Dunlop, A. Singh, J. M. Allen, P. J. Weddle, J. I. Preimesberger, J. Coyle, A. M. Colclasure, Z. Yang, B. J. Ingram and A. N. Jansen, *ACS Appl. Energy Mater.*, 2023, **6**, 9243–9248.
19 J. Joos, M. Ender, I. Rotscholl, N. H. Menzler and E. Ivers-Tiffée, *J. Power Sources*, 2014, **246**, 819–830.
20 J. Bareño, I. A. Shkrob, J. A. Gilbert, M. Klett and D. P. Abraham, *J. Phys. Chem. C*, 2017, **121**, 20640–20649.
21 C. Pereira-Nabais, J. Światowska, A. Chagnes, F. Ozanam, A. Gohier, P. Tran-Van, C.-S. Cojocaru, M. Cassir and P. Marcus, *Appl. Surf. Sci.*, 2013, **266**, 5–16.
22 S. K. Heiskanen, J. Kim and B. L. Lucht, *Joule*, 2019, **3**, 2322–2333.
23 E. Peled, D. Golodnitsky and G. Ardel, *J. Electrochem. Soc.*, 1997, **144**, L208.
24 S.-Y. Sun, N. Yao, C.-B. Jin, J. Xie, X.-Y. Li, M.-Y. Zhou, X. Chen, B.-Q. Li, X.-Q. Zhang and Q. Zhang, *Angew. Chem., Int. Ed.*, 2022, **61**, e202208743.
25 W. Yu, K.-Y. Lin, D. T. Boyle, M. T. Tang, Y. Cui, Y. Chen, Z. Yu, R. Xu, Y. Lin, G. Feng, Z. Huang, L. Michalek, W. Li, S. J. Harris, J.-C. Jiang, F. Abild-Pedersen, J. Qin, Y. Cui and Z. Bao, *Nat. Chem.*, 2025, **17**, 246–255.
26 C.-T. Lechtenfeld, J. Buchmann, J. Hagemeister, M. M. Bela, S. van Wickeren, S. Stock, R. Daub, S. Wiemers-Meyer, M. Winter and S. Nowak, *Adv. Sci.*, 2024, **11**, 2405897.
27 S. Klein, P. Bärmann, L. Stolz, K. Borzutzki, J.-P. Schmiegel, M. Börner, M. Winter, T. Placke and J. Kasnatscheew, *ACS Appl. Mater. Interfaces*, 2021, **13**, 57241–57251.
28 F. Dai, R. Yi, H. Yang, Y. Zhao, L. Luo, M. L. Gordin, H. Sohn, S. Chen, C. Wang, S. Zhang and D. Wang, *ACS Appl. Mater. Interfaces*, 2019, **11**, 13257–13263.
29 H. Sohn, D. H. Kim, R. Yi, D. Tang, S.-E. Lee, Y. S. Jung and D. Wang, *J. Power Sources*, 2016, **334**, 128–136.